Effect of Mechanical Stress Tensor on Phase Equilibria in Body-Centered Interstitial Alloys: Case of Carbon-Supersaturated Iron

Philippe Maugis

Effect of mechanical stress tensor on phase equilibria in body-centered interstitial alloys – Case of carbon-supersaturated iron

Philippe Maugis[0000−0001−9283−0471]

Aix Marseille University, CNRS, IM2NP, Marseille, France
philippe.maugis@im2np.fr

Abstract. Solid solutions in Fe–C, Fe–N, Nb–O, Ta–O or W–C systems consist of a body-centered lattice containing C, N or O interstitials in octahedral sites. Among these systems, carbon-supersaturated iron has a major industrial interest. At low temperature, it can be found in the form of ferrite (bcc-Fe) or martensite (bct-Fe and bco-Fe). Based on a mean-field elasto-chemical model of the interstitial–strain interaction, we investigated numerically the thermodynamic stability of the three possible crystal forms. The phase stability depends not only on temperature and solute carbon content but also on the mechanical stress state of the crystal. We computed phase diagrams mapping the equilibrium phase and orientational variant as function of the components of the stress tensor. These maps are intended to help understanding the spatial distribution of orientational variants in martensite nano-crystals and in Cottrell atmospheres around dislocations.

Keywords: elasticity · long-range ordering · carbon steels · mean-field modeling.

1 Introduction

C, N and O atoms in group VB (V, Nb, Ta), group VIB (Cr, Mo, W) and in α-Fe solid solutions are located in octahedral interstices of the body-centered metal lattice. In the crystal lattice, the two metallic atoms nearest to an interstitial atom are displaced along direction-1, 2 or 3 of the crystal cell, depending on the type of the interstice (1, 2 or 3). This displacement sets up a local distortion of the crystal in the form of a strain field of tetragonal symmetry. The elastic interaction energy between the strain fields is minimized when all interstitial atoms occupy the same type of site. This results in the Zener ordering phenomenon [37,14]: (i) at low temperature, most interstitials sit in a single type of site, and the phase is tetragonal bct-martensite; (ii) at high temperature, the interstitials occupy evenly the three types of sites, and the phase is cubic bcc-ferrite. Through interaction with the interstitial-induced strain field, an applied stress field can modify the site-energies: uniaxial tension along direction-3, for instance, favors sites-3, while compression favors sites 1 and 2 [29,17]. As a consequence, the occupation probabilities at equilibrium depend on the magnitude of the axial stress. This is the origin of the well known Snoek relaxation phenomenon [30]. Applied stress may also lead to uneven distribution of interstitials over the sites, i.e. the beyond-Zener ordering, stabilizing the orthorhombic bco-martensite phase [18,19]. More generally, one would expect that all components of an applied stress tensor affect the site occupancy, depending on interstitial content and temperature. The temperature–composition phase diagram is thus expected to depend on the applied stress tensor, and ordering transitions may occur upon changing the stress.

The purpose of the present work was to build a general theory of ordering transitions caused by C, N or O atoms in body-centered metals, and to explore the effect of applied stress on the temperature–stress phase diagrams related to the solid solutions. Such an investigation is needed for a better understanding of the role of stresses on the onset of martensitic nano-structures. Indeed, martensite nano-structures consist of three types of ordered domains, called orientational variants α_1, α_2 and α_3, delimited by antiphase boundaries [15,36]. The spatial distribution of these variants is likely to be affected by the internal stresses in cases of Cottrell atmospheres [34,7], white etching areas [26], highly-drawn perlite [8,17] or expanded martensite [5], etc.

In this work, we relied on the elasto-chemical model of the thermodynamics of body-centered solid solutions developed by Maugis [18]. We built the Gibbs energy function of ordering, and computed a series of temperature–stress 3D diagrams, isotherms, temperature–stress 2D sections and related temperature–strain diagrams. The theory is summarized in Section 2, and the results are presented in Section 3.

2 The elasto-chemical model

The elasto-chemical model is a mean-field thermodynamic description of long-range ordering in body-centered crystals. It accounts for the strain-induced long-range interactions, neglecting short-range interactions and magnetic effects. The model accounts for Zener ordering [22,24], carbon diffusion [21] and thermo-elasticity in bcc-ferrite and bct-martensite [18,19]. It renders quantitatively the Snoek peak of ferrite [20,23] and martensite [25]. The main features of the model are described below, details can be found in Ref. [18].

2.1 The stressed crystal

Thermodynamic equilibrium of a mechanically stressed crystal corresponds to the minimum of the Gibbs energy function $G = H - TS$, where T is the temperature, S the entropy and H the enthalpy. Under uniform mechanical stress described by tensor $\boldsymbol{\sigma}$, the enthalpy is written $H = U - V\boldsymbol{\sigma}\cdot\boldsymbol{\varepsilon}$, where U is the internal energy, V is the crystal volume and $\boldsymbol{\varepsilon}$ is the homogeneous strain as reference to the stress-free state. In the absence of plasticity, phase transition or chemical reactions, the crystal strain is a linear function of the stress (Hooke's law), viz. $\boldsymbol{\varepsilon} = \boldsymbol{S}\boldsymbol{\sigma}$, with $\boldsymbol{S}$ the mechanical compliance tensor of the crystal.

Compared to a pure crystal, solute atoms are also known to induce lattice strains. The magnitude of the strain depends on the volume concentration of the solutes and on their distribution over the lattice sites. In the simplest case, the strain is a dilation or a contraction, which follows Vegard's law. More generally, the strain is described by a tensor comprising isotropic and deviatoric components. Within the theory of linear elasticity of point defects [2,1], a solute is considered as a point source of stress, described by a force dipole tensor $\boldsymbol{P}$. In a deformed crystal, the elastic interaction energy between the defect and the strain field $\boldsymbol{\varepsilon}$ is written $-\boldsymbol{P}\boldsymbol{\varepsilon}$. A collection of solute atoms induce the anelastic strain $\boldsymbol{S}\boldsymbol{p}$, where $\boldsymbol{p}$ is the volume density of force dipole tensors. Under applied stress $\boldsymbol{\sigma}$ the total relaxed strain of a solid solution is then $\boldsymbol{\varepsilon} = \boldsymbol{S}\,(\boldsymbol{\sigma} + \boldsymbol{p})$. From this relationship, we see that the dipole density tensor acts as an internal stress of magnitude $\boldsymbol{p}$. The contribution of elasticity to the enthalpy of the crystal can then be expressed as [21]

$$H = -\frac{1}{2}V\boldsymbol{S}(\boldsymbol{\sigma}+\boldsymbol{p})\cdot(\boldsymbol{\sigma}+\boldsymbol{p}). \tag{1}$$

In the following, we establish the symmetrized Hooke's law by taking advantage of the cubic symmetry of the host lattice. We define the long-range structural order parameters and the force dipole tensors. After that, the enthalpy is written as a function of the symmetrized stress components and the order parameters. Introduction of the configurational entropy leads to the expression of the Gibbs energy function.

2.2 Symmetrized Hooke's law

In this section, we establish a simple, decoupled, constitutive law of crystals of cubic symmetry. We assume that the elastic constants of the interstitial solid solution are not strongly dependent on the interstitial content. This is true for carbon contents up to 12.5 at% in iron [31,12]. Hence, a relatively accurate description of the elastic response of body-centered interstitial crystals can be achieved by using the elasticity coefficients of the host lattice. On account of its crystal symmetry, the bcc lattice has three independent compliance components: S_{11}, S_{12} and S_{44}. Indices 1, 2 and 3 refer to the crystal directions of the cubic cell. To take further advantage of the cubic symmetry, one introduces the symmetrized stresses and strains defined as [27]

$$\begin{cases} p = -\frac{1}{3}(\sigma_{11}+\sigma_{22}+\sigma_{33}) \\ \sigma = \sigma_{33} - \frac{1}{2}(\sigma_{11}+\sigma_{22}) \\ \tau = \frac{1}{2}(\sigma_{22}-\sigma_{11}) \end{cases} \tag{2}$$

and

$$\begin{cases} \frac{\Delta V}{V} = \varepsilon_{11}+\varepsilon_{22}+\varepsilon_{33} \\ \varepsilon = \varepsilon_{33} - \frac{1}{2}(\varepsilon_{11}+\varepsilon_{22}) \\ \gamma = \varepsilon_{22} - \varepsilon_{11} \end{cases} \tag{3}$$

p is the hydrostatic pressure; σ is the 'longitudinal' stress along direction-3 counter-balanced by the 'transversal' stresses along directions 1 and 2. It will be referred to as the tetragonal stress; τ is the shear stress in

the plane rotated by 45° around direction 3. $\frac{\Delta V}{V}$ is the relative volume change; ε quantifies the tetragonal distortion along direction-3; finally, γ is the shear strain in the plane rotated by 45° around direction-3. The advantage of the symmetrized stresses and strains is that they are decoupled. Indeed, the anisotropic Hooke's law $\boldsymbol{\varepsilon} = \boldsymbol{S\sigma}$ translates into a simple, diagonal relationship between symmetrized variables:

$$\begin{cases} \frac{\Delta V}{V} = -3(S_{11} + 2S_{12})p \\ \varepsilon = (S_{11} - S_{12})\sigma \\ \gamma = 2(S_{11} - S_{12})\tau \\ 2\varepsilon_{23} = S_{44}\sigma_{23} \\ 2\varepsilon_{13} = S_{44}\sigma_{13} \\ 2\varepsilon_{12} = S_{44}\sigma_{12} \end{cases} \tag{4}$$

Notice that each symmetrized strain is directly proportional to its corresponding symmetrized stress. The proportionality coefficients involve the symmetrized compliances, defined as

$$\begin{cases} S = S_{44} \\ S' = 2(S_{11} - S_{12}) \\ S'' = S_{11} + 2S_{12} \end{cases} \tag{5}$$

From Equation 4, we see that $3S''$ is the bulk compressibility of the crystal, and S' is the shear compliance at 45° around direction-3.

2.3 The body-centered crystal

In the body-centered solid solutions under consideration, soluted interstitial atoms occupy the three sublattices of octahedral sites (Fig. 1, left). Partial occupancy of the sublattices is described in the mean-field approach by the interstitial/substitutional fractions c_i, $i = 1, 2, 3$. For a given total fraction c, a distribution of interstitial atoms over the sublattices is quantified by two non-conservative structural order parameters, η and ζ such that

$$\begin{cases} c = c_1 + c_2 + c_3 \\ c\eta = c_3 - \frac{1}{2}(c_1 + c_2) \\ c\zeta = c_2 - c_1 \end{cases} \tag{6}$$

Notice that the relationship defining the three parameters c, η and ζ follows the same scheme as the symmetrized stresses and strains. Parameter η quantifies the degree of Zener order along crystal direction [001], while ζ quantifies the unequal occupancy of the sites in directions [100] and [010].

The state of order of a distribution of interstitials is characterized by the pair of parameters (η, ζ). In the case $(1, 0)$, for instance, all interstitial atoms sit on sublattice-3. This configuration represents a tetragonal, fully ordered orientational variant, whose tetragonality axis is along [001]; it is labeled Z3. Couples $(-0.5, -1)$ and $(-0.5, 1)$ represent the Z1 and Z2 variants, fully ordered along directions [100] and [010] respectively, see Fig. 1, right. Couple $(0, 0)$ is the fully disordered cubic structure, with equal occupancy of the three sublattices. Intermediate values of (η, ζ) are partially ordered orthorhombic structures, of which there are six variants [3].

Highly ordered variants are instances of the martensite phase. They can be grouped into three couples, according to the most occupied sublattice (major ordering), labeled α_1, α_2 and α_3. Sub-variants can be defined by the second most occupied sublattice (minor ordering). For instance, major variant α_3 has two minor variants α_{3_1} and α_{3_2}. Notice that tetragonal bct-martensite is a particular case of orthorhombic bco-martensite. Low-order variants are instances of the ferrite phase, labeled α. Cubic bcc-ferrite is a particular case of orthorhombic bco-ferrite.

2.4 Force dipole tensors

Each interstitial atom produces an elastic field characterized by its force dipole tensor $\boldsymbol{P}^{(i)}$, where $i = 1, 2, 3$ labels the sublattice. As the octahedral sites are tetragonal in symmetry, the dipole tensors consist of a

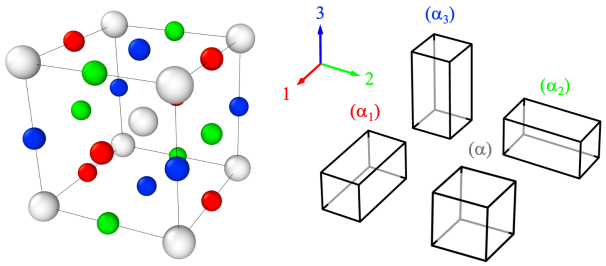

Fig. 1. Left: Body-centered crystal cell. Substitutional atoms are represented by gray spheres, octahedral sites by colored spheres. Sites of type 1, 2, 3 are respectively in color red, green, blue. Right: Schematics of ferrite α and martensite variants α_1, α_2 and α_3.

singlet value P_c in the direction of the dipole, and a doublet value P_a in the transverse directions:

$$\boldsymbol{P}^{(1)} = \begin{bmatrix} P_\mathrm{c} & 0 & 0 \\ 0 & P_\mathrm{a} & 0 \\ 0 & 0 & P_\mathrm{a} \end{bmatrix} \quad \boldsymbol{P}^{(2)} = \begin{bmatrix} P_\mathrm{a} & 0 & 0 \\ 0 & P_\mathrm{c} & 0 \\ 0 & 0 & P_\mathrm{a} \end{bmatrix} \quad \boldsymbol{P}^{(3)} = \begin{bmatrix} P_\mathrm{a} & 0 & 0 \\ 0 & P_\mathrm{a} & 0 \\ 0 & 0 & P_\mathrm{c} \end{bmatrix} \tag{7}$$

The tensor components verify $P_\mathrm{c} > P_\mathrm{a} > 0$, such that an interstitial atom induces a prolate tetragonal distortion to the crystal. The volume density of force dipole tensor is expressed as $\boldsymbol{p} = \frac{1}{V_0}\sum c_i \boldsymbol{P}^{(i)}$, where V_0 is the atomic volume of the host lattice. As mentioned in Section 2.1, interstitial atoms contribute by the strain $\boldsymbol{Sp}$ to the total deformation of the crystal, as reference to the cubic interstitial-free state: $\boldsymbol{\varepsilon} = \boldsymbol{S}\,(\boldsymbol{\sigma} + \boldsymbol{p})$. Introducing the symmetrized stress components and the order parameters, the total relaxed strain is written

$$\begin{cases} \frac{\Delta V}{V} &= -3S''p + \frac{V_\mathrm{C}}{V_0}c \\ \varepsilon &= \frac{1}{2}S'\sigma + \frac{V_\Sigma}{V_0}c\eta \\ \gamma &= S'\tau + \frac{V_\Sigma}{V_0}c\zeta \end{cases} \tag{8}$$

and $2\varepsilon_{ij} = S\sigma_{ij}$, $i \neq j$. We see that the tetragonal distortion ε is related to the order parameter η, while the shear strain γ is related to the order parameter ζ. Thus, a change in the order parameters produces a change in crystal shape, but no change in crystal volume. The volume change is controlled by the total interstitial content, irrespective of the distribution of the atoms over the sublattices. As an example, if all interstitial atoms are distributed in sublattice-3 ($\eta = 1, \zeta = 0$), the crystal is tetragonally strained along direction-3. On the other hand, if interstitial atoms are evenly distributed over the three sublattices ($\eta = 0, \zeta = 0$), the crystal remains cube-shaped, but expanded. In the general case, the crystal shape is orthorhombic, since each crystal direction is differently expanded (positively or negatively).

The above equations are the constitutive law of the bcc solid solution. They involve two characteristic volumes quantifying the interstitial-induced strain:

$$\begin{cases} V_\mathrm{C} = (S_{11} + 2S_{12})(P_\mathrm{c} + 2P_\mathrm{a}) \\ V_\Sigma = (S_{11} - S_{12})(P_\mathrm{c} - P_\mathrm{a}) \end{cases} \tag{9}$$

V_C (positive) is the relaxation volume of an interstitial atom. V_Σ (also positive) quantifies the interstitial-induced tetragonality. These volumes are related to the strain-concentration parameters λ_1 and λ_2 by $V_\mathrm{C} = (\lambda_1 + 2\lambda_2)V_0$ and $V_\Sigma = (\lambda_1 - \lambda_2)V_0$.

Each interstitial atom on sublattice i interacts elastically with the strain $\boldsymbol{\varepsilon}$, with an interaction energy $-\boldsymbol{P}^{(i)} \cdot \boldsymbol{\varepsilon}$ [2,1]. Via this interaction, the total strain favors one (or two) sublattice(s) at the expense of the others. Upon applying an external stress, a net flux of solutes sets up from one sublattice to the others, thus modifying the interstitial distribution and consequently changing the crystal strain. That is the origin of the anelastic behavior of Fe-C ferrite, manifested by an internal friction signal [27,4,20,23,18]. In addition, interstitial atoms interact elastically with one another via the interstitial-induced strain. At high solute content or low temperature, this stabilizes the Zener-ordered bct crystal, i.e. the martensite phase, where the solute atoms tend to occupy the same sublattice [37,14,24]. This coupling between strain and solute distribution is the driving force for phase transitions under applied stress, as will be shown in the following sections.

2.5 Alloy thermodynamics

For a given distribution of solute atoms over the interstitial sites, the enthalpy per substitutional atom is the sum of three contributions (Eq. 1): $H = -\frac{1}{2}V_0\boldsymbol{S}(\boldsymbol{\sigma}\cdot\boldsymbol{\sigma} + 2\boldsymbol{\sigma}\cdot\boldsymbol{p} + \boldsymbol{p}\cdot\boldsymbol{p})$. The first term is the elastic enthalpy $H^{\sigma\sigma}$, the second term is the interstitial–stress interaction enthalpy $H^{\sigma\mathrm{p}}$ and the third term is the interstitial–interstitial interaction energy H^{pp}. Introducing the symmetrized stresses p, σ and τ, and the order parameters η and ζ, we find the analytical forms

$$H^{\sigma\sigma} = -V_0\left[\frac{3}{2}S''p^2 + \frac{1}{2}S'\left(\frac{\sigma^2}{3}+\tau^2\right) + \frac{1}{2}S(\sigma_{23}^2+\sigma_{13}^2+\sigma_{12}^2)\right] \tag{10}$$

$$H^{\sigma\mathrm{p}} = -c\left[-V_{\mathrm{C}}p + 2V_\Sigma\left(\frac{\sigma\eta}{3}+\frac{\tau\zeta}{2}\right)\right] \tag{11}$$

$$H^{\mathrm{pp}} = -c^2\left[h_{\mathrm{C}} + 3h_\Sigma\left(\frac{\eta^2}{3}+\frac{\zeta^2}{4}\right)\right] \tag{12}$$

The above expressions involve the strain-energy parameters quantifying the interstitial–interstitial elastic interaction:

$$\begin{cases} h_{\mathrm{C}} = \frac{1}{6V_0}(S_{11}+2S_{12})(P_{\mathrm{c}}+2P_{\mathrm{a}})^2 \\ h_\Sigma = \frac{1}{3V_0}(S_{11}-S_{12})(P_{\mathrm{c}}-P_{\mathrm{a}})^2 \end{cases} \tag{13}$$

We see that the elastic enthalpy $H^{\sigma\sigma}$ is independent of the fraction of interstitials c. It expands into a quadratic form of the symmetrized stresses. The interstitial–stress interaction enthalpy $H^{\sigma\mathrm{p}}$, however, is proportional to the solute fraction. It shows three independent stress–interstitial couplings: the total solute fraction c couples with the pressure p, such that an increase in pressure favors a decrease in solute fraction. This results from the positive sign of the relaxation volume of the interstitial, V_{C}, which renders the increase in crystal volume with solute addition. Notice that the hydrostatic pressure does not couple with the order parameters, such that pressure has no effect on ordering. The tetragonal stress σ couples with order parameter η, such that a tensile stress along direction 3 favors Zener ordering in the same direction, i.e. it favors variant α_3. Last, the shear stress τ couples with order parameter ζ, such that a positive shear stress favors variant α_2, while a negative shear stress favors variant α_1. Finally, the interstitial–interstitial interaction enthalpy H^{pp} is proportional to the square of the solute fraction. It decreases quadratically with the order parameters, favoring the fully ordered states as compared to partially ordered or disordered states [24]. From the above expressions, the ordering enthalpy function is written

$$\Delta H = -2V_\Sigma c\left(\frac{\sigma\eta}{3}+\frac{\tau\zeta}{2}\right) - 3h_\Sigma c^2\left(\frac{\eta^2}{3}+\frac{\zeta^2}{4}\right). \tag{14}$$

We introduce the configurational entropy of as the sum of contributions of each sublattice considered as disordered. For solute contents up to $\sim 10\%$, the dilute approximation $S = -k_{\mathrm{B}}[c_1\ln c_1 + c_2\ln c_2 + c_3\ln c_3]$ is accurate enough [22]. From this expression, the ordering entropy function writes in full

$$\Delta S = -\frac{1}{3}k_{\mathrm{B}}c\left[\left(1-\eta-\frac{3}{2}\zeta\right)\ln\left(1-\eta-\frac{3}{2}\zeta\right) + \left(1-\eta+\frac{3}{2}\zeta\right)\ln\left(1-\eta+\frac{3}{2}\zeta\right) + (1+2\eta)\ln(1+2\eta)\right]. \tag{15}$$

Function ΔS is proportional to the solute fraction, and is stress independent. Predictably, the entropy is maximum in the fully disordered state ($\eta = \zeta = 0$) and minimum for fully ordered variants Z1, Z2 and Z3. From the expressions of ΔH and ΔS we conclude that, although the stress tensor contains 6 independent components, the ordering Gibbs energy function $\Delta G = \Delta H - T\Delta S$ depends on two symmetrized stresses only, namely $\sigma = \sigma_{33} - \frac{1}{2}(\sigma_{11}+\sigma_{22})$ and $\tau = \frac{1}{2}(\sigma_{22}-\sigma_{11})$. Pressure plays no role on interstitial ordering, no more so than the shear stresses σ_{12}, σ_{23} and σ_{13}. Thus, iso-concentration phase diagrams, as presented in the following sections, will be three-dimensional T–σ–τ graphs.

3 Results

Let us recall that our investigation is focused on the solid solution, i.e. the interstitial atoms are assumed to remain dissolved in the matrix, such that no unmixing or precipitation is accounted for. However, due to the

existence of three interstitial sublattices, upon changing solute content, temperature or applied stress, the distribution of solute atoms over the sublattices evolves, resulting eventually in ferrite–martensite phase transition or martensite variant flip. Such changes are reflected by changes in the internal variables, accompanied by crystal strains.

In the following sections, we report 3D temperature–stress phase diagrams, isotherms and iso-stress phase diagrams. The temperature and stress dependence of the internal variables is also analyzed.

3.1 Methods

Under fixed solute interstitial content c, temperature T and stresses σ and τ, the equilibrium state of the solid solution corresponds to the minimum of the Gibbs energy function G. In a single phase, internal equilibrium is reached when the internal variables η and ζ verify the set of equations

$$G_\eta = G_\zeta = 0, \tag{16}$$

where the subscripts denote partial derivation. The analytical forms of the partial derivatives of G can be found in Appendix A. Equations 16 are the implicit equations defining the equilibrium state of order as function of the external variables C, T, σ and τ.

Coexistence of two phases, labeled 1 and 2 for instance, occurs when the external variables are such that $G(\eta_1, \zeta_1) = G(\eta_2, \zeta_2)$. This equality, together with the conditions of internal equilibrium $G_\eta(\eta_1, \zeta_1) = G_\zeta(\eta_1, \zeta_1) = G_\eta(\eta_2, \zeta_2) = G_\zeta(\eta_2, \zeta_2) = 0$, determine the phase boundary. In a three-dimensional T–σ–τ graph at given solute content c, the phase boundaries consist of 2D surfaces. These surfaces meet at triple lines, along which three phases coexist. Triple lines may eventually meet at quadruple points, where four phases coexist.

A single phase is stable with respect to small variations of the order parameters as long as $G_{\zeta\zeta} \geq 0$ and $\mathcal{L} \geq 0$. Definition of function $\mathcal{L}$ involves the second derivatives of G [11,6]:

$$\mathcal{L} = G_{\eta\eta} G_{\zeta\zeta} - G_{\eta\zeta}^2. \tag{17}$$

Notice that condition $G_{\zeta\zeta} \geq 0$ is verified when $\mathcal{L} \geq 0$ is true [6]. Therefore, when crossing the co-existence surface from phase-1 to phase-2, phase-1 remains metastable as long as $\mathcal{L} \geq 0$. Equation $\mathcal{L} = 0$, together with Equations 16, thus define a spinodal surface in the T–σ–τ graph.

Two spinodal surfaces associated to a given phase boundary join and tangent one another along critical lines. Critical lines verify Equations 16 together with $\mathcal{L} = 0$ and $\mathcal{M} = 0$. Function $\mathcal{M}$, involving second and third derivatives of G, is defined as [11]:

$$\mathcal{M} = G_{\eta\eta\eta} G_{\zeta\zeta}^2 - 3 G_{\eta\eta\zeta} G_{\zeta\zeta} G_{\eta\zeta} + 3 G_{\eta\zeta\zeta} G_{\eta\zeta}^2 - G_{\zeta\zeta\zeta} G_{\eta\eta} G_{\eta\zeta}. \tag{18}$$

Critical lines imply the existence of supercritical regions: a critical line between phases 1 and 2 is the rim of the co-existence surface, beyond which the first-order phase transition $1 \leftrightarrow 2$ becomes continuous.

Critical lines may eventually meet and tangent one another at critical points. These points were systematically sought in this study.

3.2 The Gibbs energy function

From the analytical expression of the Gibbs energy function, reduced variables can be defined, such that the properties of all bcc systems with octahedral interstitials follow a unified description, independent of the material parameters. As far as ordering is concerned, the pertinent material parameters are h_Σ and V_Σ defined in Sections 2.4 and 2.5. For the reduced variables, the units of temperature, stress and energy are respectively: $h_\Sigma c/k_\mathrm{B}$, $h_\Sigma c/V_\Sigma$ and $h_\Sigma c^2$, where k_B is Boltzmann's constant. Among the latter, units of temperature and stress are proportional to the interstitial fraction c. Hence, temperature–stress diagrams, when drawn with variables T/c, σ/c and τ/c are valid for any interstitial fraction. In the specific case of Fe–C system, we adopted the parameters computed by density functional theory calculations [9], from which $h_\Sigma = 2.91\,\mathrm{eV}$ and $V_\Sigma = 6.79 \times 10^{-5}\,\mathrm{eV/MPa}$. Then, for a solute carbon content of $c = 1\,\mathrm{at\%}$ ($0.215\,\mathrm{wt\%C}$), the units of temperature, stress and energy are respectively $338\,\mathrm{K}$, $428\,\mathrm{MPa}$ and $0.291\,\mathrm{meV}$. In the following,

reduced variables will be noted with a star '*' superscript. Hence, reduced variables convert to normal ones via the following relationships: $T = 338cT^*$ (in K), $\sigma = 428c\sigma^*$ (in MPa) and $H = 0.291c^2H^*$ (in meV), with c in at%. With the reduced variables, the reduced Gibbs energy of ordering is written:

$$\begin{aligned}\Delta G^* = -2\left(\frac{\sigma^*\eta}{3} + \frac{\tau^*\zeta}{2}\right) - 3\left(\frac{\eta^2}{3} + \frac{\zeta^2}{4}\right) \\ +\frac{1}{3}T^*\left[\left(1-\eta-\frac{3}{2}\zeta\right)\ln\left(1-\eta-\frac{3}{2}\zeta\right) + \left(1-\eta+\frac{3}{2}\zeta\right)\ln\left(1-\eta+\frac{3}{2}\zeta\right) + (1+2\eta)\ln(1+2\eta)\right]\end{aligned} \tag{19}$$

From this equation, contour maps in the (η, ζ) plane can be computed at fixed c and T (which sets the value of T^*), and for various stresses σ^* and τ^*. Examples are presented in Fig. 2 at high reduced temperature ($T^* = 1.5$, top row), which correspond to high temperature or low solute content, and at low reduced temperature ($T^* = 0.9$, bottom row), which corresponds to low temperature or high solute content. At $T^* = 1.5$, the low-order α-ferrite phase is stable; Under positive tetragonal stress the equilibrium state is shifted towards positive values of η (Fig. 2b); Under positive shear stress, the equilibrium state is shifted towards positive values of ζ (Fig. 2c). At $T^* = 0.9$, high-order α_i-martensite variants are stabilized; If no stress is applied, the three variants α_1, α_2 and α_3 are equally stable (Fig. 2d). Under positive tetragonal stress the stable variant is α_3, while variants α_1 and α_2 are metastable (Fig. 2e). The opposite occurs, i.e. variants α_1 and α_2 are stabilized, under negative tetragonal stress (Fig. 2f); Under positive shear stress the stable variant is α_2 (Fig. 2g); Symmetrically, the stable variant is α_1 under negative shear stress (Fig. 2h).

3.3 Temperature–stress 3D phase diagrams

We have established that the stress tensor enters the ordering Gibbs energy function via the two symmetrized stresses σ and τ. Besides, the effect of interstitial content is contained in the reduced intensive variables T^*, σ^* and τ^*. Hence, a single master T^*–σ^*–τ^* phase diagram can inform on the effect of interstitial content, temperature and stress on the equilibrium state of the solid solution. The variables T, σ and τ are potentials, since they are intensive variables that must be uniform at equilibrium [11]. Therefore, in the T–σ–τ phase diagram, co-existence of two phases occurs along surfaces, which eventually end along critical lines, and critical lines join at critical points. Spinodals are surfaces, which join along critical lines.

We computed the T^*–σ^*–τ^* phase diagram from the equations of internal equilibrium, of co-existence surfaces, of spinodal surfaces and of critical lines, as described in Section 3.1. A large-scale view of the diagram is presented in Fig. 3, top left. Its shape sketches a three-fold lamppost. The three-fold aspect arises from the symmetry of the cubic crystal around direction [111]. Four domains appear: (α_1), (α_2) and (α_3) martensite variants at low temperature, and ferrite (α) at high temperature. As expected, high temperature favors the low-order ferrite phase, whereas low temperature favors the high-order martensite phase. Martensite variants are separated by three planar vertical co-existence surfaces (traces on the box faces are figured by dashed lines). The co-existence surfaces join along a triple line on the zero-stress vertical axis. The upper rim of each co-existence surface is a critical line. Transitions across a co-existence surfaces are first-order. Conversely, a transformation path going over a critical line transits through the supercritical region, such that the transition is continuous.

A close view to the diagram reveals the ferrite–martensite co-existence surfaces (Fig. 3, top right and bottom left). This lily-flower-shaped region consists of three slightly curved triangular-shaped co-existence surfaces, each of them bounded by two triple lines and a critical line. All four triple lines of the diagram join on the zero-stress axis at quadruple point Q, at temperature $T^*_{\mathrm{Q}} = \frac{3}{4\ln 2} \simeq 1.082$. Pairs of critical lines join and tangent at critical points K_{12}, K_{23} and K_{13} where they merge with a critical line of variant-variant transition. Transitions across the α–α_i co-existence surfaces are first-order, whereas $\alpha \leftrightarrow \alpha_i$ transitions over the critical lines are continuous. Since the ferrite and martensite domains are all topologically connected, we can assess that ferrite and the three martensite variants are actually the same phase.

The symmetry of the T–σ–τ phase diagram reflects the cubic symmetry of the host lattice. Indeed, ordering transitions must remain similar when the normal stresses σ_{11}, σ_{22} and σ_{33} are permuted. It follows that any point of coordinates (τ, σ, T) has a correspondence at coordinates $\left(\frac{1}{2}(-\sigma \pm \tau), \frac{1}{2}(-\sigma \mp 3\tau), T\right)$ and $\left(\frac{1}{2}(\sigma \pm \tau), \frac{1}{2}(-\sigma \pm 3\tau), T\right)$. Hence, the graph is three-fold and has the $\tau \leftrightarrow -\tau$ mirror symmetry.

The mirror symmetry of the state diagram implies that the boundary between martensite variants α_1 and α_2, and the associated critical line, are located in the plane $\tau = 0$ corresponding to $\zeta = 0$. This remark

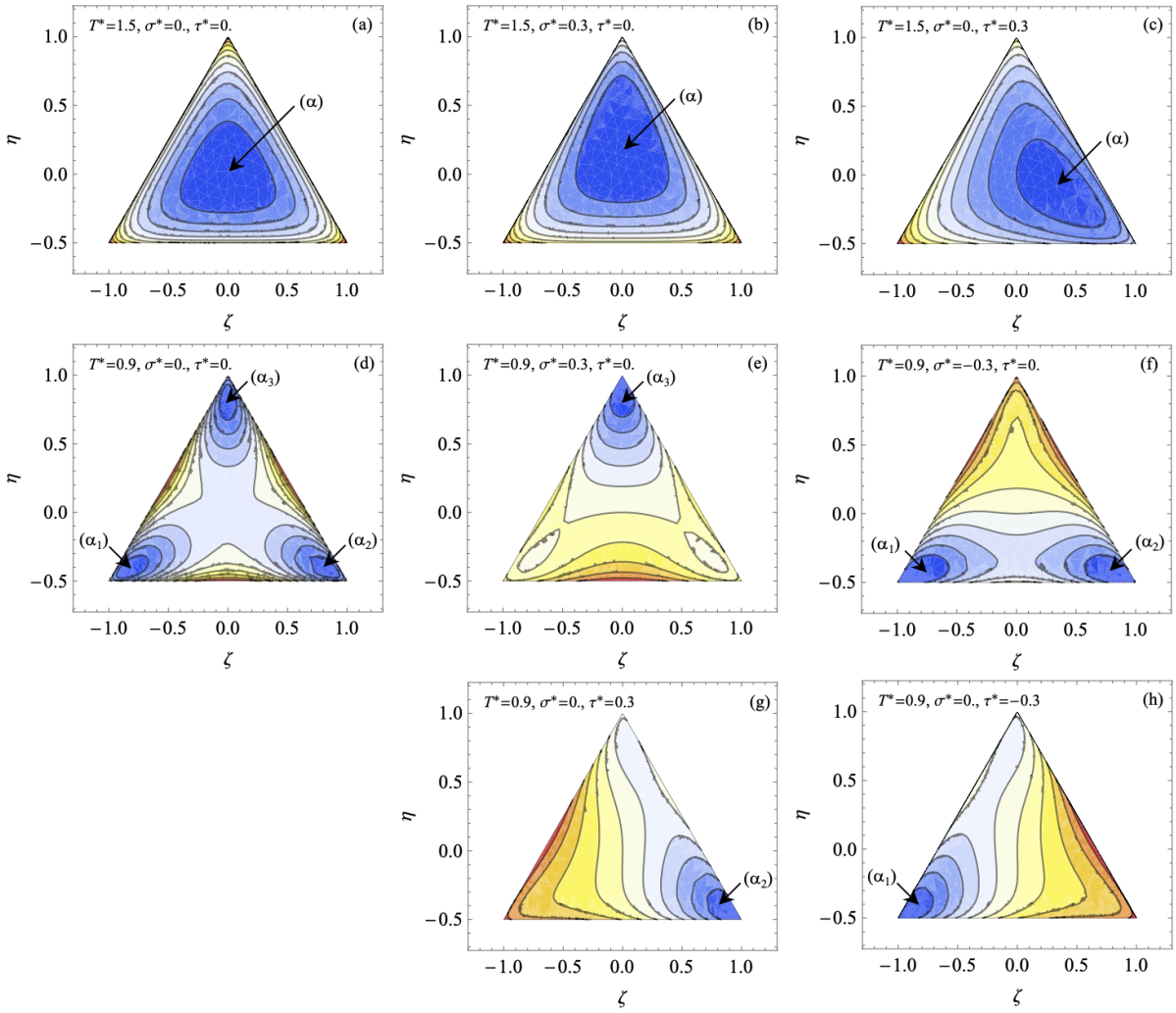

Fig. 2. Contour maps of the Gibbs energy function, for two reduced temperatures T^* and various stresses σ^* and τ^*, as function of order parameters η and ζ. The arrows point to the positions of absolute minima. Low-order ferrite (α) is stable at high temperature (top row); high-order martensite variants (α_i) are stable at low temperature (middle and bottom rows). The nature of the stable martensite variant, α_1, α_2 or α_3, depends on the applied stress.

allows for an analytical analysis of the boundary. Solving the set of equations $G_\eta = G_\zeta = \mathcal{L} = \mathcal{M} = 0$, we find the equation of the critical line:

$$\sigma^*(T^*) = -3 + (3 + \ln 2)T^* + T^* \ln\left(\frac{\frac{3}{2} - T^*}{T^*}\right). \tag{20}$$

The branch between temperature $T^*_{\mathrm{K}} = \frac{7}{6}$ at point K_{12} and the asymptotic value $T^*_\infty = \frac{3}{2}$ is the upper rim of the α_1–α_2 co-existence surface. Hence, stress-induced change of variant may occur discontinuously when $T^* < 1.5$, but is necessarily continuous when $T^* > 1.5$. Critical point K_{12} is located at coordinates $\tau^*_{K_{12}} = 0$, $\sigma^*_{K_{12}} = \frac{1}{2} + \frac{7}{6}\ln\frac{4}{7} \simeq -0.153$ and $T^*_{\mathrm{K}} = \frac{7}{6} \simeq 1.167$. The other critical points are also at temperature T^*_{K} and stresses $\tau^*_{K_{23,13}} = \pm\frac{1}{2}\sigma^*_{K_{12}} \simeq \pm 0.076$ and $\sigma^*_{K_{23,13}} = -\frac{1}{2}\sigma^*_{K_{12}} \simeq 0.076$.

The branch of Equation 20 located between $T^*_- = 1$ at point K_- and $T^*_{\mathrm{K}} = \frac{7}{6}$ is not a critical line. It verifies the set of equations $G_\eta = G_\zeta = \mathcal{L} = 0$ for $\tau = 0$, but not $\mathcal{M} = 0$. It is the intersection of two spinodal surfaces that limit the domain of metastability of α-ferrite, i.e. an edge of this domain. The three edges are colored in orange in Fig. 3, bottom left. Together with the critical lines in orange in the figure, they draw

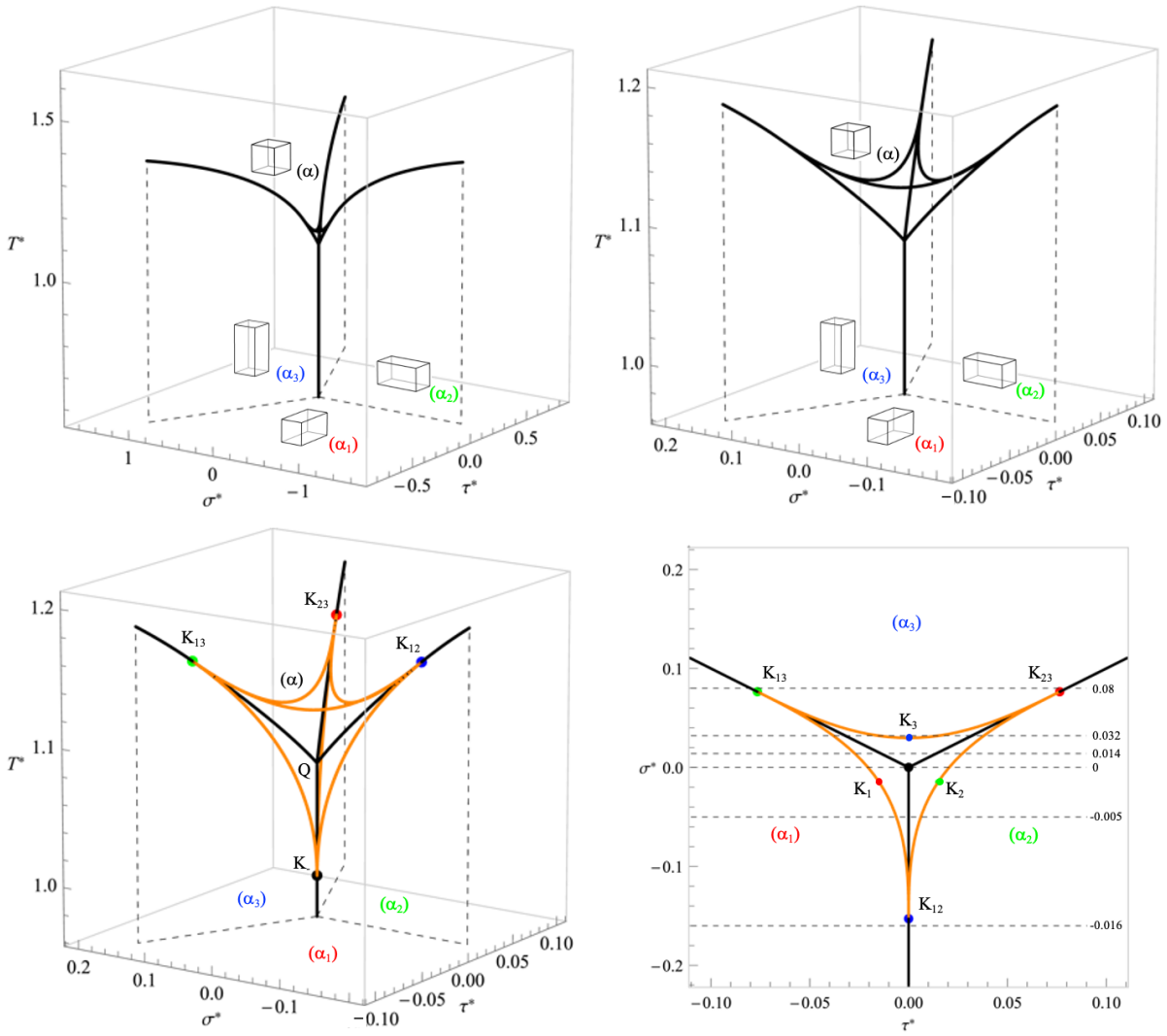

Fig. 3. Temperature–stress 3D diagrams. Top left: large-scale view (the three-fold lamppost). Top right: close view of the central zone (the three-fold lily flower). Bottom left: close view showing the edges of the spinodal surfaces related to α-ferrite, in orange. K_{12}, K_{23}, K_{13} and K_- are the critical points, Q is the quadruple point. Bottom right: polytherm projection, dashed lines are traces of the iso-stress sections presented in Figs. 6 and 7.

the spinodal surface associated to ferrite. The low-temperature point of this domain is the critical point K_- located on the zero-stress axis at temperature $T^*_- = 1$.

The polytherm projection of the diagram is presented in Fig. 3, bottom right. We define points K_1, K_2 and K_3 situated at the minima of the α–α_i critical lines. Their common temperature is $T^*_{K_i} = \frac{9}{8} = 1.125$. Point K_3 is at stress $\tau^*_{K_3} = 0$, $\sigma^*_{K_3} = -\frac{3}{4} + \frac{9}{8}\ln 2 \simeq 0.0298$. Iso-stress sections described later in Sections 3.5 and 3.5 are indicated as dashed lines.

3.4 Isothermal σ–τ sections

In a two-dimensional section, the phases boundaries are lines, which eventually end at critical points. The limits of metastability are also lines, ending at critical points. We computed a series of isothermal sections of the equilibrium phase diagram. At the same temperatures, ordering maps were computed by minimizing the Gibbs energy function. The results are described below.

Isothermal σ–τ ordering maps. Isotherms presented in Fig. 4 map the equilibrium state of order as a function of the stresses σ and τ, for a set of selected temperatures. The red, green and blue intensities were set proportional to the site fractions c_1, c_2 and c_3 respectively. Hence, martensite domains are red, green or blue depending on the variant, while ferrite domain is gray. The couples of order parameters (η,ζ) were computed by minimizing the Gibbs energy function, starting from the fully disordered state (0,0). As a consequence, the map reveals the limits of metastability of ferrite. We see that ferrite (α) is stable or metastable at high temperature. Upon cooling, it is destabilized to the benefit of one of the martensite variants (α_i). Below $T^* = 1$, ferrite is unstable, whatever the stress.

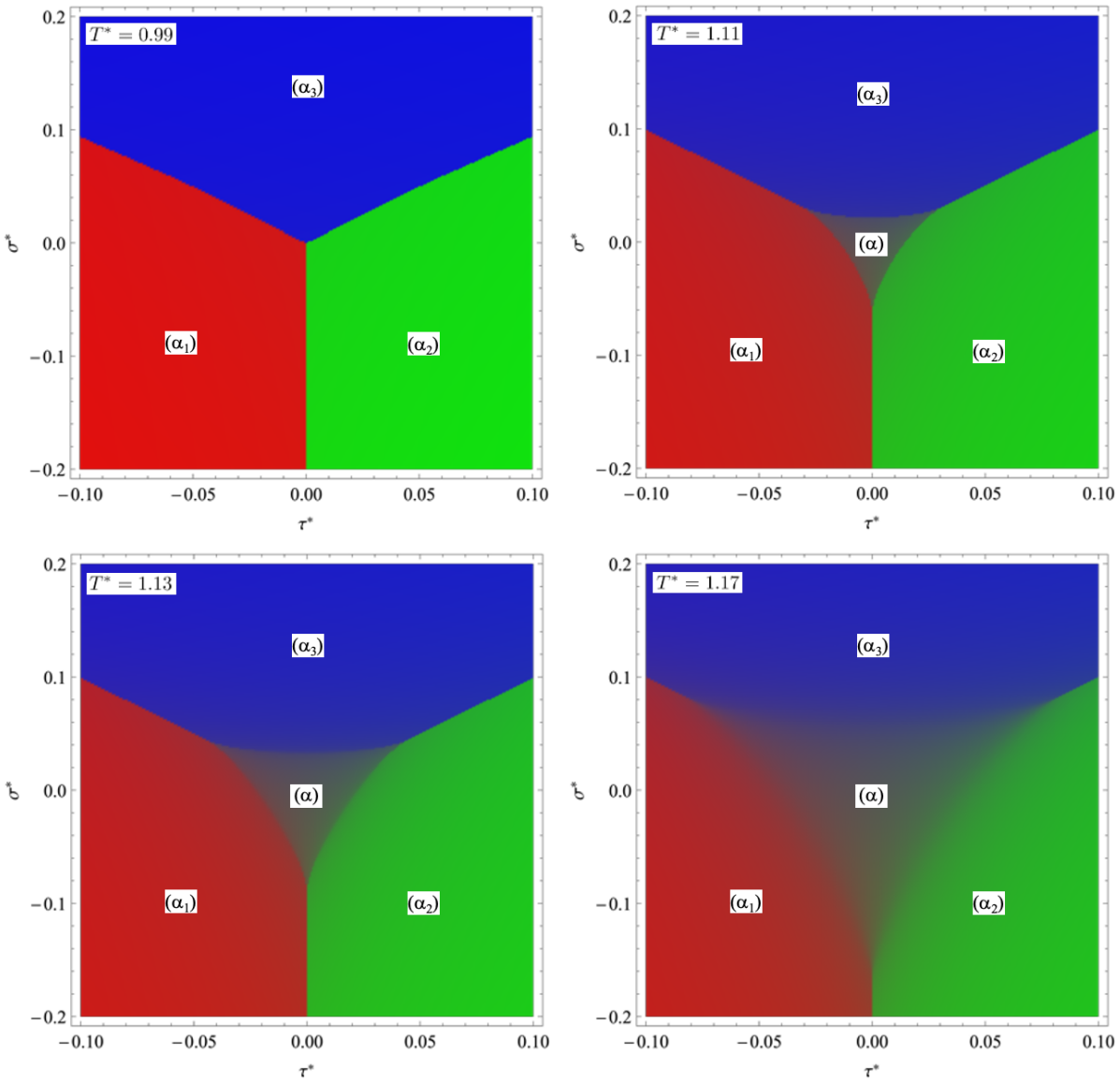

Fig. 4. Isothermal σ–τ ordering maps computed by Gibbs energy minimization. The RGB intensities were set proportional to the site fractions c_i. Martensite domains appear red, green or blue according to the major variant, while ferrite is gray. At high temperature, the ferrite–martensite domain boundaries are diffuse, indicating continuous ferrite $\leftrightarrow$ martensite ordering transitions.

At a given temperature, first-order transitions between martensite variants are visualized by abrupt change in color at domain boundaries. At $T^* = 1.11$, the ferrite–martensite boundaries are also abrupt, indicating first-order stress-induced transitions. However, at $T^* = 1.17$ the ferrite–martensite boundaries are diffuse, which is the sign of continuous transitions. $T^* = 1.13$ is an intermediate temperature, where the ferrite–martensite boundaries are abrupt in the corners of the ferrite domain, but diffuse elsewhere.

Isothermal σ–τ sections of phase diagram. The ordering maps of Fig. 4 can be matched with the isothermal sections of the phase diagram, Fig. 5. Four temperature intervals were distinguished:

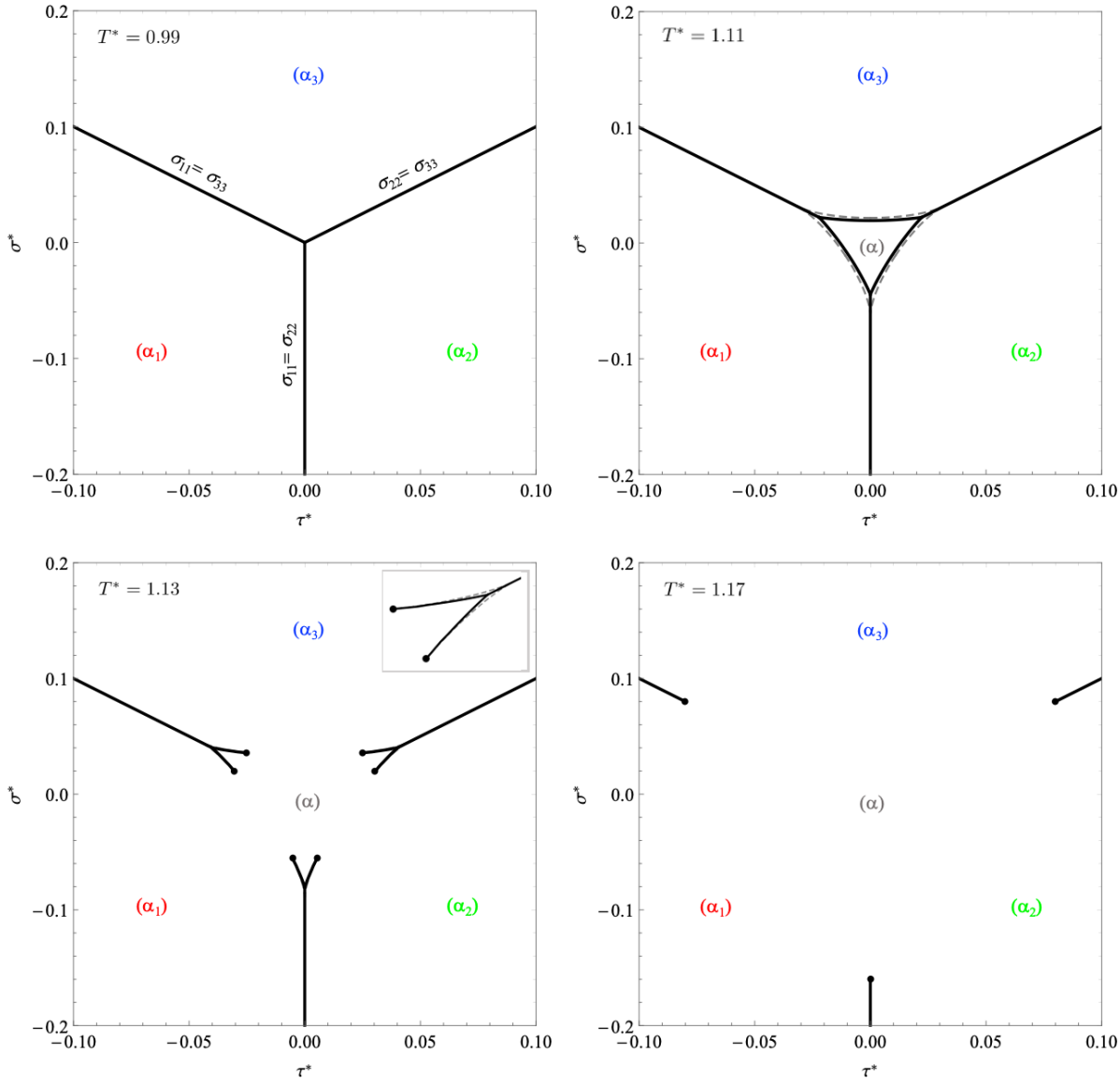

Fig. 5. Isothermal σ–τ sections of the phase diagram. Co-existence lines are solid lines, spinodal lines of ferrite are dashed lines, and critical points are black circles. The states of order corresponding to these diagrams are presented in Fig. 4.

$T < T_-$. Temperature $T^* = 0.99$ is below the temperature of the quadruple point, $T^*_{\mathrm{Q}} \simeq 1.082$. Consequently, the isothermal section only contains the three martensite variants. $T^* = 0.99$ is also below the temperature under which ferrite is unstable, $T^*_- = 1$. Thus, ferrite does not appear in the ordering map (Fig. 4). The martensite variants are distributed over three sectors. The sector boundaries correspond to the equality of two normal stresses. This provides a simple rule for martensite variant selection: *the stable variant α_i has its major axis i oriented along the direction of the highest normal stress σ_{ii}*. For instance, the upper sector of the isotherm, defined by $\sigma_{33} > \sigma_{11}, \sigma_{22}$, delineates variant α_3. More, for each major variant, the minor variant is selected by the second highest normal stress: in the upper sector, the right-hand zone corresponds to α_{3_2} and the left-hand zone to α_{3_1}, and so on for the other sectors. Computation of the order parameters (not shown here) proves that the transition between minor variants (e.g. $\alpha_{3_1} \leftrightarrow \alpha_{3_2}$) is neither first-order nor second-order, but is continuous. The change of major variant, however, is first-order since it is accompanied by a discontinuity in order parameters η and ζ, which corresponds to a discontinuity in the crystal strain.

$T_{\mathrm{Q}} < T < T_{\mathrm{K_i}}$. The section at temperature $T^* = 1.11$ is above the quadruple point, $T^*_{\mathrm{Q}} \simeq 1.082$, but below the critical line that borders the ferrite–martensite coexistence surface. In fact, the minima along the critical line are located at $T^*_{\mathrm{K_i}} = 1.125$. The triangular-shaped ferrite domain lies in the low-stress central region. In this section, all ferrite $\leftrightarrow$ martensite transitions are first-order. Ferrite is metastable beyond the co-existence line, in the region delineated by the spinodal line (dashed line): this latter line coincides with the boundary of the gray domain in the ordering map (Fig. 4).

$T_{\mathrm{K_i}} < T < T_{\mathrm{K}}$. The section at $T^* = 1.13$ is above $T^*_{\mathrm{K_i}} = 1.125$ but below the critical points, $T^*_{\mathrm{K}} \simeq 1.167$. Consequently, the section intersects the ferrite–martensite critical line on 6 locations, which are the critical points of the section (black points in Fig. 5). Intersection with the co-existence surface generates Y-shaped co-existence lines. In the present range of temperature, the ferrite $\leftrightarrow$ martensite transition is continuous everywhere, except in the corners of the Y's, where is it first-order. Correspondingly, the contrast is abrupt in the corners of the ordering map (Fig. 4) and diffuse elsewhere. Two spinodal lines of ferrite are presented in the enlargement. They end at critical points, tangentially to the co-existence line.

$T_{\mathrm{K}} < T$. Temperature $T^* = 1.17$ of this section is above the critical points, $T^*_{\mathrm{K}} \simeq 1.167$. The section intersects the variant–variant critical lines at three points. In the central part of the section, where the stress is low, ferrite $\leftrightarrow$ martensite and variant $\leftrightarrow$ variant transitions are continuous. The corresponding boundaries in the ordering map are diffuse. The transitions are first-order in the outer part of the section, where the stress magnitude is high.

3.5 Iso-stress sections of phase diagram

In the following section, equilibria and phase transitions under specific stress states are examined, based on iso-stress sections of the phase diagram. Temperature–shear stress diagrams were computed in reduced units (T^*–τ^*) for higher generality. Temperature–shear strain diagrams (T–γ) were computed in the case of a Fe–C solid solution.

Iso-stress T–τ sections. Fig. 6 presents a series of sections of the phase diagram computed at specific values of the tetragonal stress σ^*. Traces of the sections are shown as dashed lines in the polytherm projection (Fig. 3). Values of σ^* were selected in relation to the characteristic points of the 3D phase diagram, which we recall here: $\sigma^*_{K_{12}} \simeq -0.153$ at the critical point K_{12} on the "compressive" part of the diagram; $\sigma^* = 0$; $\sigma^*_{\mathrm{K_3}} \simeq 0.0298$ at the minimum of the K_{13}–K_{23} critical line; and $\sigma^*_{K_{23,13}} \simeq 0.0765$ at the critical points $K_{23,13}$ on the "tensile" part of the diagram. All iso-σ diagrams are symmetrical about the $\tau^* = 0$ axis. These diagrams consist of co-existence lines (solid lines), eventually ending at critical points, and spinodal lines (dashed lines). The dashed lines colored in red, green, blue and gray are the limits of metastability of the phases α_1, α_2, α_3 and α respectively.

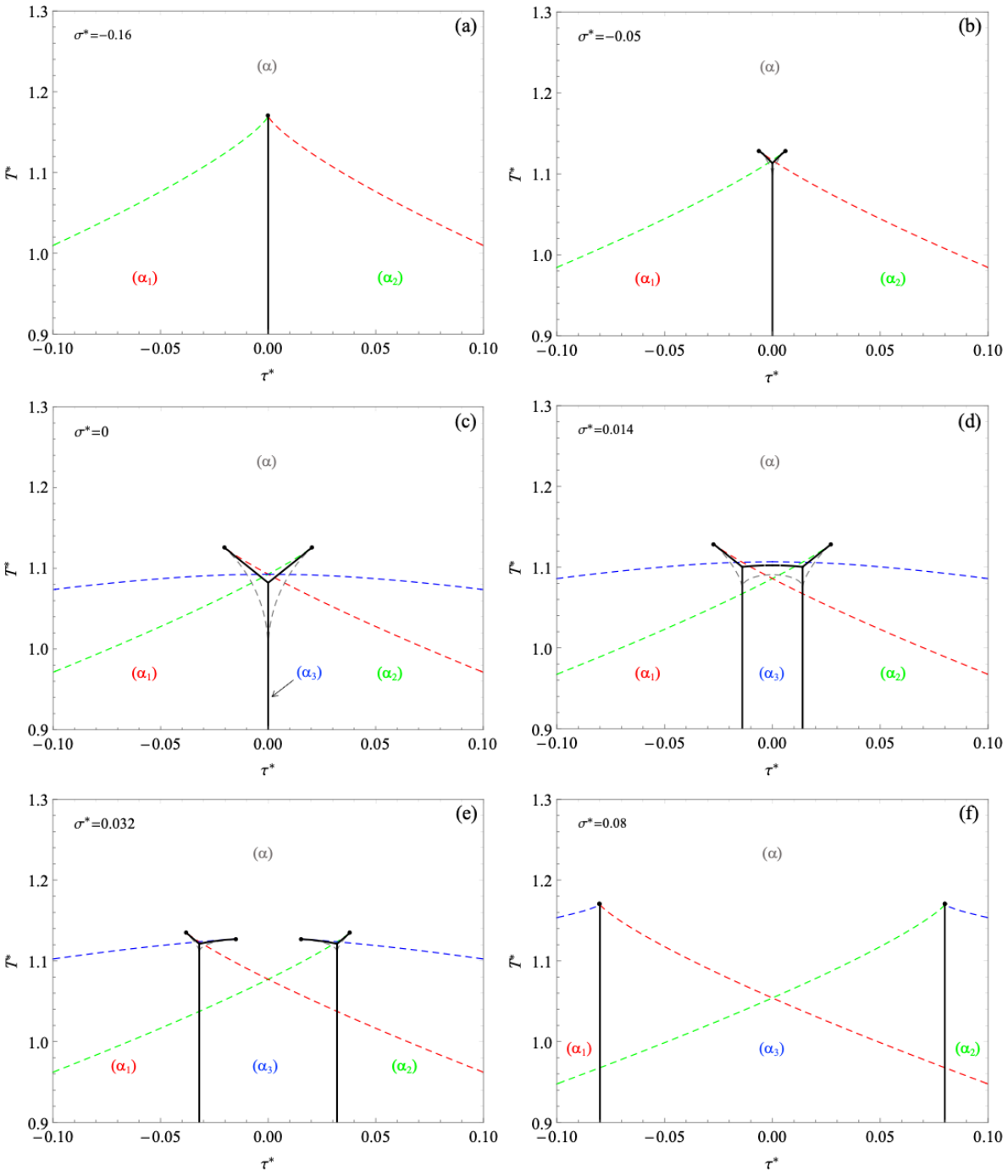

Fig. 6. T–τ sections at various tetragonal stress σ^* (refer to Fig. 3 for locations in the polytherm projection). The dashed lines colored in red, green, blue and gray are the spinodal lines of the phases α_1, α_2, α_3 and α respectively.

Iso-stress T–γ sections. The relationship $\tau = (1/V)\partial G/\partial\gamma$ shows that the shear strain γ is the conjugate variable of the shear stress τ. Temperature–strain (T–γ) phase diagrams were constructed as conjugate of the temperature–stress (T–τ) diagrams by using the expression of the relaxed strain (Eq. 8): $\gamma = S'\tau + \frac{V_\Sigma}{V_0}C\zeta$, where ζ is the order parameter at equilibrium. The first term of this sum is the elastic unrelaxed strain, while the second term is the anelastic strain induced by the unequal distribution of the solute atoms over

sublattice-1 and -2. In the low-order state, the anelastic strain is weak, but it is predominant in the high-order state. Parameters S' and V_Σ/V_0 entering the equation are specific to a given system, such that no universal diagram can be drawn. In this study, we focused on the Fe–C system, whose parameters were computed from density functional theory [9]: $S' = 1.49 \times 10^{-5}$ MPa^{-1} and $V_\Sigma/V_0 = 0.959$. With these parameters, the anelastic shear strain in fully ordered martensite variants is about 1% per atomic percent of solute carbon.

On account of the discontinuity of order parameter ζ at first-order transitions, the shear strain γ is discontinuous at the transitions. Hence, each co-existence line in the T–τ diagram corresponds to a gap in the T–γ diagram. The shear strains on both sides of the gap are the equilibrium strains of the phases situated on both sides of the co-existence line. The T–γ phase diagrams in Fe-1 at%C are presented in Fig. 7. They correspond to the T–τ phase diagrams of Fig. 6. On the strain axis, the reference $\gamma = 0$ is stress-free ferrite. For the alloy under consideration, conversion from reduced to real values follows the relationships $T = 338\,T^*$ (in K), $\sigma = 428\,\sigma^*$ and $\tau = 428\,\tau^*$ (in MPa). Hence, the characteristic stresses in the phase diagrams are of the order of a few tens of MPa.

$\boldsymbol{\sigma < \sigma_{K_{12}}}$. When σ^* is negative and less than $\sigma_{K_{12}}$, the T–τ section has the form of a unique co-existence line in the plane $\tau^* = 0$, see Fig. 6a. The upper part of the co-existence line ends at a critical point, which is the trace of the critical line passing through point K_{12} in the 3D diagram. On the left-hand side of the co-existence line, variant α_1 is stabilized by the negative shear stress, whereas variant α_2 is stabilized by the positive shear stress on the right-hand side. α-ferrite is stable at high temperature. The $\alpha_1 \leftrightarrow \alpha_2$ transition is first-order below the critical temperature, but continuous if the transformation path goes around the critical point, through the supercritical region. The spinodal lines join and tangent at the critical point, as a rule in a potential diagram [33]. Such a diagram is similar to what was observed in Fe-31.2%Pd alloy [35] and in fcc-cerium metal [16]. The conjugate T–γ diagram has the classical form of a miscibility gap (Fig. 7a). The critical point in T–τ space corresponds to the maximum in T–γ space, where co-existence lines and spinodal lines tangent one another. The miscibility gap corresponds to the discontinuity in shear strain during an $\alpha_1 \leftrightarrow \alpha_2$ transition. Notice that, from Eq. 8, this discontinuity in strain has the peculiarity of producing no volume change ($\Delta V = 0$). Furthermore, the enthalpy change is null at the transition ($\Delta H = 0$). This is because, along the co-existence line, both variants are symmetrical with reference to the stress tensor, such that the enthalpy contribution of the strain-stress interaction, $-\boldsymbol{p\varepsilon}$, is the same for both variants. On account of the Clapeyron relationship, we have $d\tau/dT = 0$, i.e. the co-existence line is vertical [19]. From this, we can identify the whole co-existence line as a Kauzmann line [32,13].

$\boldsymbol{\sigma_{K_{12}} < \sigma \leq 0}$. In this range of stress, T–τ sections have a characteristic Y-shape resulting from the intersection of the section plane with the ferrite–martensite co-existence surfaces, in addition to the α_1–α_2 co-existence plane, see Fig. 6b and c. The ferrite $\rightarrow$ martensite first-order transitions through the upper branches of the "Y" are associated with two spinodal lines (in gray), which join on the $\alpha_1 \leftrightarrow \alpha_2$ co-existence line. The corresponding T–γ diagram presents a two-peak miscibility gap (Fig. 7b). This type of phase diagram was predicted theoretically by Landau [16], and defined as "homotectoid" by Okamoto [28]. The two maxima in T–γ space correspond to the two critical points in T–τ space; the triple line along which α, α_1 and α_2 phases co-exist corresponds to the triple point. The section at $\sigma^* = 0$ is singular. In fact, at $\sigma^* = \tau^* = 0$, stress-free martensite is tetragonal and stress-free ferrite is cubic; the tetragonal $\leftrightarrow$ cubic transition occurs at the triple point upon temperature change (as a contrast, all other transitions in the phase diagram occur between orthorhombic structures). In addition, variant α_3 is also part of the section at $\sigma = 0$, but only along the $\tau = 0$ line, which is the trace of the triple line of the T–σ–τ phase diagram (Fig. 3). Such a situation corresponds to the contour plot of function G drawn in Fig. 2d, where the three martensite variants are degenerate. The spinodal lines of the three martensite variants cross at temperature $T_+^* = 1.0926$, which is the limit of metastability of stress-free martensite upon heating (Fig. 6c). As a complement, a discussion of the thermo-elastic response of the Fe–C solid solution at $\sigma = 0$, based on the present iso-stress section, can be found in Ref. [23].

$\boldsymbol{0 < \sigma < \sigma_{K_3}}$. When the tetragonal stress σ is positive, the iso-σ plane passes through three variant domains and crosses two variant–variant co-existence surfaces. If in addition, σ is less that σ_{K_3}, the plane also crosses a portion of the ferrite–martensite co-existence surface. The T–τ section then consists of two

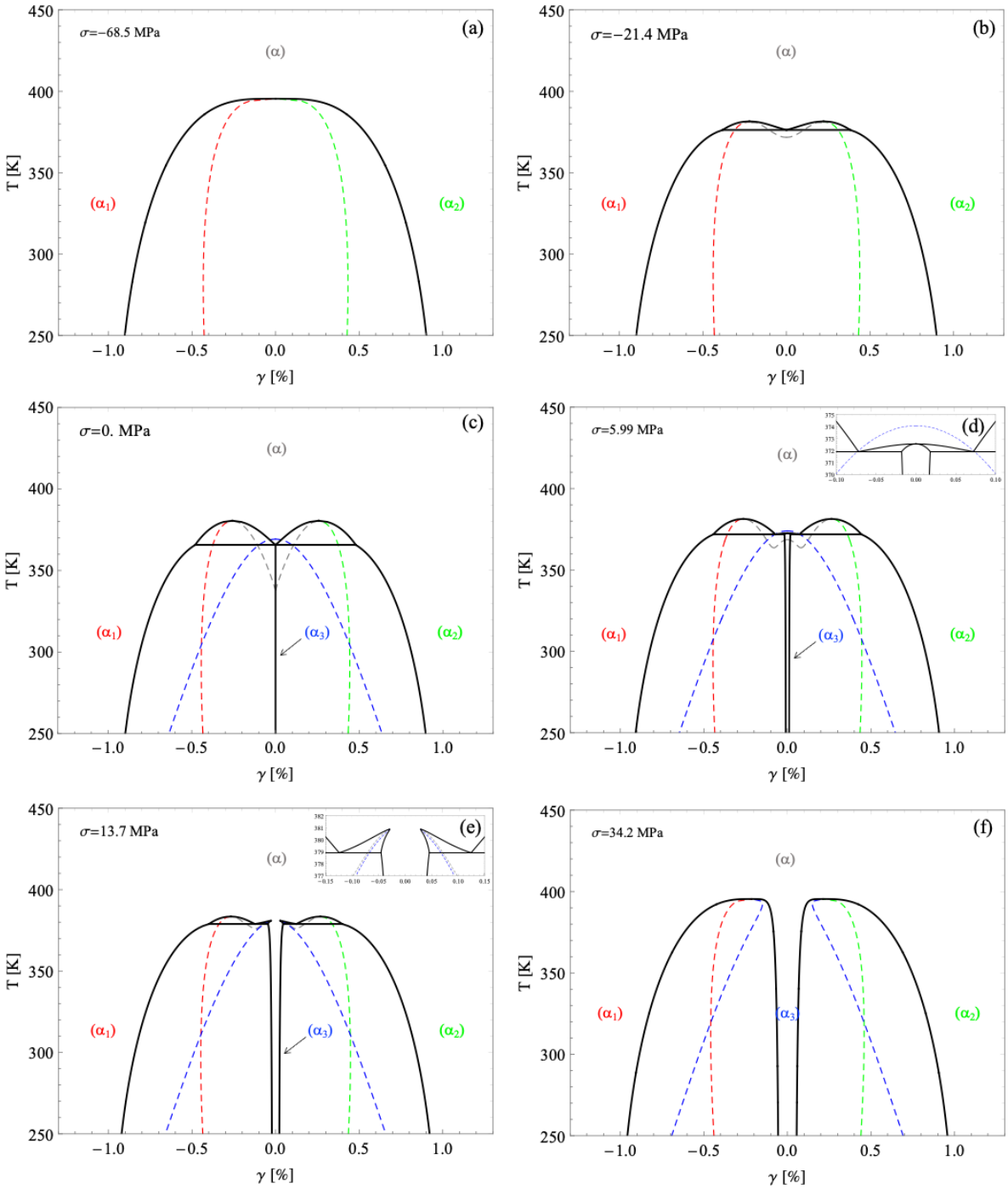

Fig. 7. T–γ sections for the alloy Fe-1 at%C. These sections are conjugate to the T^*–τ^* sections of Fig. 6. The colored dashed lines (red, green, blue and gray) are the spinodal lines of the corresponding phases (α_1, α_2, α_3 and α).

interconnected Y's, and a close stability domain of α_3 appears (Figs. 6d and 7d). At low temperature, one of the three martensite variants is stable, depending on the shear stress. If the shear stress is close to zero, variant α_3, whose major axis is along direction-3, is stabilized by the tetragonal tensile stress σ. Beyond its domain of stability, α_3 is metastable until its spinodal line is reached (blue dashed line in Figs. 6d and 7d). Upon applying a shear stress, the $\alpha_3 \to \alpha_2$ or $\alpha_3 \to \alpha_1$ transition occurs, depending on whether τ is positive

or negative. The diagram exhibits a congruent transformation at $\tau = 0$: at the congruent point, both α_3 and α are tetragonal, such that the order–disorder transition occurs with no change of shear strain. The tetragonal strain ε, however, undergoes a discontinuity.

$\boldsymbol{\sigma_{K_3} < \sigma < \sigma_{K_{13,23}}}$. In this range of tetragonal stress, the iso-stress plane crosses two portions of the ferrite–martensite co-existence surface. The T–τ section consists of two Y's, and the corresponding T–γ section is made of two homotectoids (Figs. 6e and 7e). We see that beyond the threshold value σ_{K_3}, the stress σ has opened the α_3 domain, such that the α_3-martensite $\leftrightarrow$ ferrite transition is no longer first-order. Although it looks like second-order (cf. [11], p. 342), the transition is continuous: it is accompanied by a continuous, however steep, change in order parameter from ordered α_3 to disordered α.

$\boldsymbol{\sigma_{K_{13,23}} < \sigma}$. Beyond the tetragonal stress $\sigma_{K_{13,23}}$, the iso-stress section shows two miscibility gaps: α_1–α_3 and α_2–α_3 (Figs. 6f and 7f). In the T–τ diagram, the co-existence lines are positioned at abscissa $\tau = \pm\sigma$: the existence domain of α_3 is all the more larger than σ is high. This is because variant α_3 is stabilized by a positive tetragonal stress. All phases are interconnected by continuous transitions. In the α_3 domain, above both α_1 and α_2 spinodals, α_3 variant is stable and variants α_1 and α_2 are unstable (Fig. 6f). Conversely, below both α_1 and α_2 spinodals, for instance at $T^* = 0.9$, variants α_1 and α_2 are metastable. Such a situation corresponds to the G contour plot of Fig. 2e.

4 Discussion and conclusion

We investigated the effect of a mechanical stress tensor on the ordering of octahedral interstitials in a body-centered lattice. In this purpose, we started from the elasto-chemical model, which describes the strain-induced elastic interactions between the interstitials. From the expression of the Gibbs energy function G, we found that the state of order of the solid solution is a function of two independent stresses only: the tetragonal stress σ and the shear stress τ. The choice of these two stresses is arbitrary, but coherent with the choice of the order parameters η and ζ describing the state of order. From function G, internal equilibrium could be computed at given interstitial content c, temperature T and stresses σ and τ. Function G allowed to build phase diagrams involving the reduced variables T^*, σ^* and τ^* derived from the potentials T, σ and τ. These phase diagrams are similar to T–μ_1–μ_2 diagrams, where μ_1, μ_2 are the chemical potentials of two solutes in a ternary solution. They are valid for any bcc lattice containing octahedral interstitials, and for any interstitial content. In that sense, they are universal. Application to a particular system (Fe–C, Fe–N, Nb–O, W–C, etc.) relies on the determination of scaling parameters for temperature and stress, respectively. Temperature–strain phase diagrams were built in the case of Fe–C system. These diagrams are topologically similar to binary temperature-composition phase diagrams, involving miscibility gaps, homotectoid topology and congruent transitions.

From the temperature–stress 3D diagram we conclude that martensite variants and ferrite are thermodynamically the same body-centered orthorhombic phase. Martensite is the high-order instance, while ferrite is the low-order instance. Temperature-induced and stress-induced transitions have been identified between these instances. We found that martensite variants are stable at temperatures less than $T^*_{\mathrm{Q}} \simeq 1.082$, whatever the stress. In a stressed crystal, the martensite $\rightarrow$ ferrite transition occurs at higher temperature, i.e. stress stabilizes the ordered state. Upon varying the temperature at constant stress, the nature of the ferrite $\leftrightarrow$ martensite transition is stress-dependent: the transition is first-order at low stress, and continuous at high stress. For isothermal transformations, at any temperature below $T^*_\infty = 1.5$, a change in stress can induce a first-order change of martensite variant. Above $T^*_\infty = 1.5$, such a change of variant is always continuous. In the temperature range between $T^*_{\mathrm{Q}} \simeq 1.082$ and $T^*_{\mathrm{K}} \simeq 1.167$, first-order ferrite $\leftrightarrow$ martensite transitions can be stress-induced. Finally, the ferrite $\leftrightarrow$ martensite transitions are necessarily continuous above $T^*_{\mathrm{K}} \simeq 1.167$.

To the author's knowledge, no experimental investigation of orientational variant stability under applied stress can be found in the literature. So, our predictions remain unconfirmed to date. Ideally, one would like to identify the change in orientation of individual variants under a known applied stress. Such an experiment is made difficult because: 1) martensite tetragonality is small (a few percent in Fe–C), such that identification of individual variant orientation is challenging; 2) knowledge of the local mechanical stress is almost impossible, due to high internal stresses in martensite. One might however get indirect

indications through low-temperature tensile–compressive tests performed on virgin martensite, coupled with in situ measurement of the crystal texture or magnetization. Indeed, both texture and magnetization are expected to vary when variant orientation flips from one crystal direction to the other. Tensile–compressive solicitations would inevitably induce plastic deformation, though. Plastic deformation of Fe–C martensite is known to occur by dislocation glide. Our theoretical investigations suggest that it may also involve a part of nano-twinning [10]. Both mechanisms are expected to interfere with carbon ordering. These phenomenons are not taken into account in the present model, but will be addressed in future work.

From our results, we infer that variant selection during martensite formation in Fe–C alloys is influenced by the local state of stress. This applies to the formation of martensite during quenching of austenite, but also to the growth of nano-variants in carbon-enriched zones such as Cottrell atmospheres and segregated grain boundaries. Future work is planed to investigate the effect of stress on the spatial distribution of orientational variants in nano-twinned Fe–C martensite.

Declaration of Competing Interest

The authors declare that they have no known competing financial interests or personal relationships that could have appeared to influence the work reported in this paper.

Acknowledgments

This work was supported by the Agence Nationale de la Recherche, France (contract C-TRAM ANR-18-CE92-0021).

A The Gibbs energy of ordering

This appendix gathers the analytic formulae related to the Gibbs energy function and its derivatives relatively to the order parameters.

The Gibbs energy for ordering $\Delta G = \Delta H - T\Delta S$ is a function of the external variables c, T, σ and τ, and of the internal variables η and ζ. It is written:

$$\begin{aligned}\Delta G = -2V_\Sigma c\left(\frac{\sigma\eta}{3}+\frac{\tau\zeta}{2}\right) - 3h_\Sigma c^2\left(\frac{\eta^2}{3}+\frac{\zeta^2}{4}\right)\\ +\frac{1}{3}k_\mathrm{B}Tc\left[\left(1-\eta-\frac{3}{2}\zeta\right)\ln\left(1-\eta-\frac{3}{2}\zeta\right)+\left(1-\eta+\frac{3}{2}\zeta\right)\ln\left(1-\eta+\frac{3}{2}\zeta\right)+(1+2\eta)\ln(1+2\eta)\right]\end{aligned} \tag{21}$$

The first derivatives of ΔG express as:

$$G_\eta = -\frac{2}{3}V_\Sigma c\sigma - 2h_\Sigma c^2\eta + \frac{1}{3}k_\mathrm{B}Tc\ln\left(\frac{(1+2\eta)^2}{\left(1-\eta-\frac{3}{2}\zeta\right)\left(1-\eta+\frac{3}{2}\zeta\right)}\right) \tag{22}$$

$$G_\zeta = -V_\Sigma c\tau - \frac{3}{2}h_\Sigma c^2\zeta + \frac{1}{2}k_\mathrm{B}Tc\ln\left(\frac{1-\eta+\frac{3}{2}\zeta}{1-\eta-\frac{3}{2}\zeta}\right) \tag{23}$$

The second derivatives are stress-independent:

$$G_{\eta\eta} = -2h_\Sigma c^2 + 2k_\mathrm{B}Tc\frac{1-\eta-\frac{3}{2}\zeta^2}{\left(1-\eta-\frac{3}{2}\zeta\right)\left(1-\eta+\frac{3}{2}\zeta\right)(1+2\eta)} \tag{24}$$

$$G_{\eta\zeta} = \frac{3}{2}k_\mathrm{B}Tc\frac{\zeta}{\left(1-\eta-\frac{3}{2}\zeta\right)\left(1-\eta+\frac{3}{2}\zeta\right)} \tag{25}$$

$$G_{\zeta\zeta} = -\frac{3}{2}h_\Sigma c^2 + \frac{3}{2}k_\mathrm{B}Tc\frac{1-\eta}{\left(1-\eta-\frac{3}{2}\zeta\right)\left(1-\eta+\frac{3}{2}\zeta\right)} \tag{26}$$

The third derivatives only contain the entropic contribution:

$$G_{\eta\eta\eta} = \frac{1}{3}k_{\mathrm{B}}Tc\left[\left(1-\eta-\frac{3}{2}\zeta\right)^{-2}+\left(1-\eta+\frac{3}{2}\zeta\right)^{-2}-8\left(1+2\eta\right)^{-2}\right] \tag{27}$$

$$G_{\eta\eta\zeta} = 3k_{\mathrm{B}}Tc\frac{(1-\eta)\zeta}{\left(1-\eta-\frac{3}{2}\zeta\right)^{2}\left(1-\eta+\frac{3}{2}\zeta\right)^{2}} \tag{28}$$

$$G_{\zeta\zeta\eta} = \frac{3}{4}k_{\mathrm{B}}Tc\left[\left(1-\eta-\frac{3}{2}\zeta\right)^{-2}+\left(1-\eta+\frac{3}{2}\zeta\right)^{-2}\right] \tag{29}$$

$$G_{\zeta\zeta\zeta} = \frac{27}{4}k_{\mathrm{B}}Tc\frac{(1-\eta)\zeta}{\left(1-\eta-\frac{3}{2}\zeta\right)^{2}\left(1-\eta+\frac{3}{2}\zeta\right)^{2}} \tag{30}$$

The expressions above were used to compute the stability limits in the phase diagrams.

References

1. Bacon, D., Barnett, D., Scattergood, R.: Anisotropic continuum theory of lattice defects. Prog. Mater. Sci. **23**, 51 (1980)
2. Balluffi, R.W.: Introduction to elasticity theory for crystal defects. Cambridge University Press (2012)
3. Bhattacharya, K.: Microstructure of martensite. Oxford University Press (2003)
4. Blanter, M., Golovin, I., Neuhauser, H., Sinning, H.R.: Internal Friction in Metallic Materials. Springer-Verlag, Berlin Heidelberg, 1st edn. (2007)
5. Borgioli, F.: The "Expanded" Phases in the Low-Temperature Treated Stainless Steels: A Review. Metals (Basel). **12**, 331 (2022)
6. C.H.P. Lupis: Chemical Thermodynamics of Materials. North-Holland, New York (1983)
7. Cochardt, A., Schoek, G., Wiedersich, H.: Interaction between dislocations and interstitial atoms in body-centered cubic metals. Acta Metall. **3**(6), 533–537 (nov 1955)
8. Djaziri, S., Li, Y., Nematollahi, G.A., Grabowski, B., Goto, S., Kirchlechner, C., Kostka, A., Doyle, S., Neugebauer, J., Raabe, D., Dehm, G.: Deformation-Induced Martensite : A New Paradigm for Exceptional Steels. Adv. Mater. **28**, 7753–7757 (2016)
9. Eyméoud, P., Huang, L., Maugis, P.: Impact of Ni alloying on Fe-C martensite ageing: an atomistic investigation. Scr. Mater. **205**, 114182 (dec 2021)
10. Eyméoud, P., Kandaskalov, D., Maugis, P.: Impact of stresses and alloying elements on ferrous martensite nanodomains. Mater. Lett. **308**(September 2021), 131248 (2021). https://doi.org/10.1016/j.matlet.2021.131248
11. Hillert, M.: Phase Equilibria, Phase Diagrams and Phase Transformations. Cambridge University Press (2007)
12. Kandaskalov, D., Maugis, P.: A first-principle study of the structural, elastic, lattice dynamical and thermodynamic properties of alpha"-Fe16C2 and alpha"-Fe16N2 phases. Comput. Mater. Sci. **128**, 278–286 (2017)
13. Kauzmann, W.: The Nature Of The Glassy State And The Behaviour Of Liquids At Low Temperatures. Chem. Rev. **43**(2), 219–256 (1948)
14. Khachaturyan, A., Shatalov, G.: On the theory of the ordering of carbon atoms in a martensite crytal. Fiz. Met. Met. **32**(1), 5–13 (1971)
15. Khachaturyan, A.G.: Theory of structural transformations in solids. Dover Publications (2008)
16. Landau, L.D., Lifshitz, E.: Statistical physics. Pergamon Press, 2nd edn. (1969)
17. Maugis, P.: Ferrite, martensite and supercritical iron: A coherent elastochemical theory of stress-induced carbon ordering in steel. Acta Mater. **158**, 454–465 (2018)
18. Maugis, P.: Nonlinear elastic behavior of iron-carbon alloys at the nanoscale. Comput. Mater. Sci. **159**, 460–469 (2019)
19. Maugis, P.: A Temperature–Stress Phase Diagram of Carbon-Supersaturated bcc-Iron, Exhibiting "Beyond-Zener" Ordering. J. Phase Equilibria Diffus. **41**, 269–275 (may 2020)
20. Maugis, P.: Giant Snoek peak in ferrite due to carbon-carbon strain interactions. Materialia **12**(8), 100805 (2020)
21. Maugis, P., Chentouf, S., Connétable, D.: Stress-controlled carbon diffusion channeling in bct-iron: A mean-field theory. J. Alloys Compd. **769**, 1121–1131 (2018)
22. Maugis, P., Danoix, F., Zapolsky, H., Cazottes, S., Gouné, M.: Temperature hysteresis of the order-disorder transition in carbon-supersaturated α-Fe. Phys. Rev. B **96**(21), 214104 (2017)
23. Maugis, P.: Thermo-kinetic modelling of the giant Snoek effect in carbon-supersaturated iron. J. Alloys Compd. **877**, 160236 (may 2021)

24. Maugis, P., Connétable, D., Eyméoud, P.: Stability of Zener order in martensite: an atomistic evidence. Scr. Mater. **194**, 113632 (2021)
25. Maugis, P., Huang, L.: Modeling the Snoek peak in bct-martensite. J. Alloys Compd. **907**, 164502 (jun 2022)
26. Mayweg, D., Morsdorf, L., Li, Y., Herbig, M.: Correlation between grain size and carbon content in white etching areas in bearings. Acta Mater. **215** (2021)
27. Nowick, A.S., Berry, B.: Anelastic relaxation in crystalline solids. Materials science series [v. 1], Academic Press, New York (1972)
28. Okamoto, H.: A two-peak miscibility gap. J. Phase Equilibria **14**(3), 336–339 (jun 1993)
29. Shtremel, M., Satdarova, F.: Influence of stresses on order in interstitial solutions. Fiz. Met. Met. **34**(4), 699–708 (1972)
30. Snoek, J.: Effect of small quantities of carbon and nitrogen on the elastic and plastic properties of iron. Physica **8**(7), 711–733 (1941)
31. Souissi, M., Numakura, H.: Elastic Properties of Fe–C and Fe–N Martensites. ISIJ Int. **55**(7), 1512–1521 (jul 2015)
32. Stillinger, F.H., Debenedetti, P.G., Truskett, T.M.: The Kauzmann Paradox Revisited. J. Phys. Chem. B **105**, 11809–11816 (2001)
33. Stølen, S., Grande, T.: Chemical Thermodynamics of Materials. John Wiley & Sons (2003)
34. Wilson, D., Russell, B., Eshelby, J.: Stress induced ordering and strain-ageing in low carbon steels. Acta Metall. **7**(9), 628–631 (1959)
35. Xiao, F., Fukuda, T., Kakeshita, T.: Critical point of martensitic transformation under stress in an Fe-31.2Pd (at.%) shape memory alloy. Philos. Mag. **95**(12), 1390–1398 (2015)
36. Yan, J.Y., Ruban, A.V.: Configurational thermodynamics of C in body-centered cubic/tetragonal Fe: A combined computational study. Comput. Mater. Sci. **147**, 293–303 (2018)
37. Zener, C.: Theory of strain interaction of solute atoms. Phys. Rev. **74**(6), 639–647 (1948)